LAWRENCE
LIVERMORE
NATIONAL
LABORATORY

UCRL-JRNL-234214

Rayleigh-Taylor Shock Waves

B. J. Olson, A. W. Cook

September 4, 2007

Physics of Fluids

Rayleigh-Taylor Shock Waves

Britton J. Olson and Andrew W. Cook

Lawrence Livermore National Laboratory, Livermore CA 94551

Abstract

Beginning from a state of hydrostatic equilibrium, in which a heavy gas rests atop a light gas in a constant gravitational field, Rayleigh-Taylor instability at the interface will launch a shock wave into the upper fluid. The rising bubbles of lighter fluid act like pistons, compressing the heavier fluid ahead of the fronts and generating shocklets. These shocklets coalesce in multidimensional fashion into a strong normal shock, which increases in strength as it propagates upwards. Large-eddy simulations demonstrate that the shock Mach number increases faster in three dimensions than it does in two dimensions. The generation of shocks via Rayleigh-Taylor instability could have profound implications for astrophysical flows.

The quest to find a detonation mechanism for type Ia supernovae has spurred many investigations of Rayleigh-Taylor (R-T) unstable flame fronts [1, 2, 3, 4, 5, 6, 7, 8, 9]. However, the vast majority of R-T simulations and experiments to date have been performed in the incompressible or low Mach number regimes. Relatively little research has been performed on the effects of compressibility and hydrostatic density gradients on the late-time development of R-T turbulence. Mellado et al. [10] studied compressibility effects in R-T turbulence in an "unbounded" domain and concluded that "the Rayleigh-Taylor problem does not have significant intrinsic compressibility ef-

fects." Their research has reinforced the perception that R-T instability is a low Mach number phenomenon. The purpose of this Brief Communication is to demonstrate that R-T instability does in fact exhibit strong compressibility effects, as evidenced by the formation of shock waves in the upper fluid.

R-T instability between two ideal gases can be described by the following equations:

$$\frac{\partial \rho Y_i}{\partial t} + \nabla \cdot (\rho Y_i \mathbf{u} + \mathbf{J}_i) = 0 \ , \quad i = 1, 2 \ , \tag{1}$$

$$\frac{\partial \rho \mathbf{u}}{\partial t} + \nabla \cdot [\rho \mathbf{u}\mathbf{u} + p\underline{\boldsymbol{\delta}} - \underline{\boldsymbol{\tau}}] = \rho \mathbf{g} \ , \tag{2}$$

$$\frac{\partial E}{\partial t} + \nabla \cdot [(E + p)\mathbf{u} - \underline{\boldsymbol{\tau}} \cdot \mathbf{u} + \mathbf{q}] = \rho \mathbf{g} \cdot \mathbf{u} \ , \tag{3}$$

$$p = \rho R T \ , \tag{4}$$

$$T = (\gamma - 1) e / R \ , \tag{5}$$

$$R = R_o \sum_{i=1}^{2} \frac{Y_i}{W_i} \ , \tag{6}$$

where ρ is density, Y_i is the mass fraction of species i, $\mathbf{u} = (u, v, w)$ is velocity, $\mathbf{J}_i$ is a diffusive mass flux, p is pressure, $\underline{\boldsymbol{\delta}}$ is the unit tensor, $\underline{\boldsymbol{\tau}}$ is the viscous stress tensor, $\mathbf{g} = (0, 0, g)$ is gravity, $E \equiv \rho(e + \mathbf{u} \cdot \mathbf{u}/2)$ is total energy (with e being internal energy), $\mathbf{q}$ is the heat conduction flux, γ is the ratio of specific heats (assumed to be the same for both gases), T is temperature, R is the apparent gas constant, R_o is the universal gas constant and W_i is a species molecular weight. The viscous stress tensor is

$$\underline{\boldsymbol{\tau}} = \mu(2\underline{\mathbf{S}}) + (\beta - \frac{2}{3}\mu)(\nabla \cdot \mathbf{u})\underline{\boldsymbol{\delta}} \ , \tag{7}$$

where μ is dynamic (shear) viscosity, β is bulk viscosity and $\underline{\mathbf{S}}$ is the symmetric

strain rate tensor,

$$\underline{\mathbf{S}} = \frac{1}{2}[\nabla \mathbf{u} + (\nabla \mathbf{u})^{\dagger}] \ , \tag{8}$$

where $(\nabla \mathbf{u})^{\dagger}$ denotes the transpose of the dyadic $\nabla \mathbf{u}$. The conductive heat flux vector is described by Fourier's law,

$$\mathbf{q} = -\kappa \nabla T \ , \tag{9}$$

where κ is thermal conductivity. The diffusive (Fickian) mass fluxes are

$$\mathbf{J}_i = -\rho D \nabla Y_i \ , \tag{10}$$

where D is the diffusion coefficient. We solve equations (1)-(10) using a tenth-order compact scheme for spatial derivatives, combined with a fourth-order Runge-Kutta integrator. In order to confine dissipation effects to the smallest possible scales, grid-dependent models are employed for μ, β, κ and D. Complete details of the numerical method and subgrid-scale models, including verification and validation tests, have previously been described [11].

In our large-eddy simulations (LES) of R-T instability, Xenon serves as the upper (heavy) fluid and Krypton, Argon or Neon serves as the lower (light) fluid. The initial mass fractions are prescribed using a hyperbolic tangent profile in z with a Gaussian spectrum of perturbations imposed at the interface [12]. The flows are initialized with isothermal fluids in hydrostatic equilibrium; i.e., we solve

$$\frac{dp}{dz} = \rho g, \tag{11}$$

together with (4), to obtain p and ρ. In all simulations, gravity is $g = -980\, cm/s^2$,

the initial temperature is $T_o = 300\,K$ and the initial pressure at the top of the domain is $p_o = 10^6\,Ba$. The boundary conditions are periodic in x and y with slip walls on the top and bottom z boundaries. As a test of the hydrostatic initialization and wall boundary conditions, simulations were conducted with no perturbations to confirm that the flow remains undisturbed.

Figure 1 depicts a time sequence of the local Mach number from a 2D LES with Argon used for the light fluid. The local Mach number is defined as

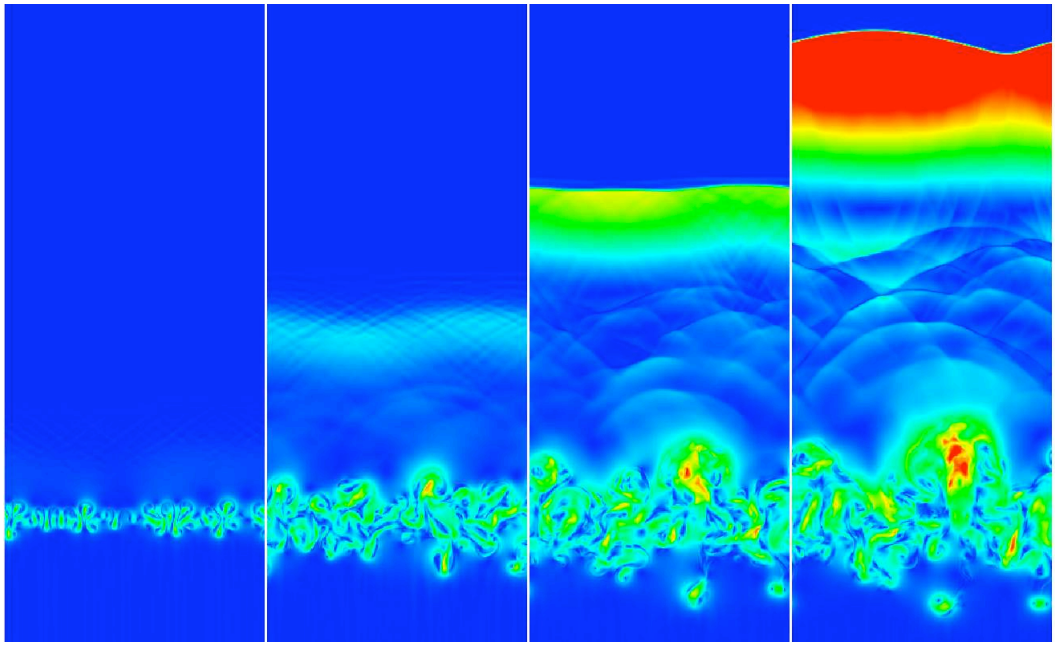

Fig. 1. Local Mach number from a 256 $\times$ 768 point simulation of compressible R-T instability. The upper fluid is Xenon and the lower fluid is Argon. The RGB color map ranges from 0 (blue) to 1 (red). The flow domain is $15.1 \times 45.4\,km$ (the full vertical extent of the computational domain somewhat exceeds that shown). Simulation times from left to right are: t=40, 80, 110 & 130 s.

$$M_l(\mathbf{x}, t) \equiv \frac{||\mathbf{u}||}{c} \ , \tag{12}$$

where $c = \sqrt{\gamma RT}$ is the local speed of sound. In the first image, only the mixing region is visible, since that is the only place where vorticity gets deposited. In the second image we begin to see compression waves emanating from the bubbles and coalescing further up in the Xenon. In the third image, curved shocklets are clearly visible above the mixing region and a main shock has formed at higher elevation. In the fourth image, the post-shock Mach number has surpassed the maximum Mach number in the mixing region and distinct shocklets fill the space between the mixing layer and the main shock. The Argon bubbles appear to act like pistons, sending compression waves into the Xenon, which catch up to previous waves, thus reinforcing the shocklets. The shocklets then combine multidimensionaly with their neighbors to form the main shock. This process is driven, in part, by expansion of the bubbles of light fluid as they rise in altitude. The process bears some resemblance to a Deflagration to Detonation Transition (DDT), where acoustic waves emanating from the reaction front combine in multidimensional fashion to form a shock. Shocklets do not form underneath the mixing region because the spikes of heavy fluid are compressed as they descend, thus sending expansion waves into the lower fluid. Furthermore, the speed of sound is larger in the lower fluid than in the upper fluid. Figure 2 shows flow features from a 3D simulation after the main shock has formed.

In constructing a model of the shock formation process, we can make direct use of the piston analogy. Consider the canonical compression wave problem wherein a piston in a 1D tube is given a constant acceleration, a [13]. The acceleration may be thought of as a series of infinitesimal velocity jumps,

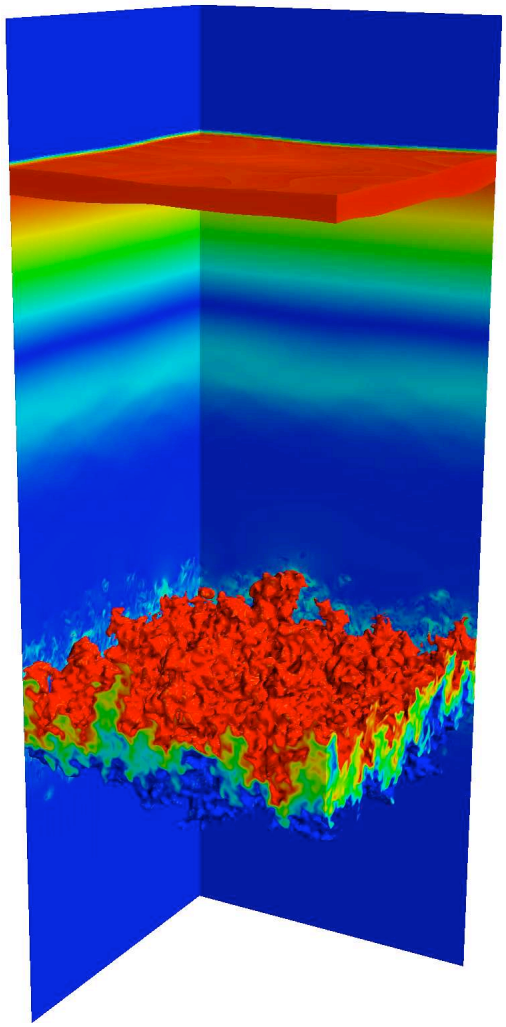

Fig. 2. Three-dimensional ($256 \times 256 \times 768$) simulation of compressible Rayleigh–Taylor instability. The top fluid is Xenon and the bottom fluid is Argon. The lower isovolume is the mixing region, where blue and red correspond to Xenon mass fractions of 0.2 and 0.8, respectively. The upper isovolume is the main shock, illustrated here by $1.04 < M_l < 1.10$. The back planes and upper isovolume are both colored by the local Mach number, where blue is 0 and red is 1.

which produce finite compression waves emanating from the piston. The first wave originates from the piston at $t = 0$ and travels at the sound speed of the undisturbed fluid, c_0. The second wave begins at $t = dt$ and travels at $c_1 + du$,

where du is the piston velocity after the first jump and c_1 is the sound speed behind the first wave. Simple compression waves satisfy the jump relation [14],

$$u_1 - \frac{2}{\gamma - 1} c_1 = u_0 - \frac{2}{\gamma - 1} c_0 \ , \tag{13}$$

which for the present case reduces to

$$c_1 = c_0 + \frac{\gamma - 1}{2} du. \tag{14}$$

The distance at which the second wave overtakes the first wave is

$$L_p = \frac{2c_0^2}{a(\gamma + 1)} \ , \tag{15}$$

where $a = du/dt$. This intersection distance for the characteristics corresponds to the location at which the shock begins to form.

The relevant acceleration for R-T instability, which appears both in Linear Stability Theory [15] and in the similarity equation for the late-time growth rate [16, 17], is Ag, where

$$A = \frac{\rho_2 - \rho_1}{\rho_2 + \rho_1} \ , \tag{16}$$

is the Atwood number. For compressible fluids, ρ_1 and ρ_2 are taken, respectively, as the local minimum and maximum of the density field on either side of the fluid interface. For the ideal gases used in the present work,

$$A = \frac{W_2 - W_1}{W_2 + W_1} \ . \tag{17}$$

Setting $a = Ag$ in (15) yields

$$L_s = \frac{2c^2}{Ag(\gamma + 1)} \tag{18}$$

as the relevant length scale for shock formation, where c is the sound speed in the upper fluid.

In order to test whether (18) is an effective gauge of the shock formation height, we performed a set of 3D simulations using Atwood numbers of 0.221, 0.533 and 0.733. These Atwood numbers correspond respectively to Krypton, Argon and Neon as the light fluid. All three simulations were performed on a $12.8\,km \times 12.8\,km \times 51.1\,km$ domain using $128 \times 128 \times 512$ grid points. The Gaussian perturbation spectrum of each simulation was centered about mode number 16. The initial fluid interface was placed one quarter of the distance from the bottom boundary to the top boundary in order to allow sufficient room for the shock to form in the Xenon. Except for the lower fluid, the simulations were all identical. Additionally, we conducted a corresponding set of 2D simulations (same perturbations and fluids etc.) in order to assess the effects of dimensionality on the shock formation process.

We define the shock location, z_s, as the z-location where $\langle T \rangle$ reaches its maximum. Here we use angle brackets to denote a horizontal (x, y) average. Figure 3 displays profiles of $\langle T \rangle$ from the 3D Argon simulation at three different nondimensional times, where

$$t_s \equiv \frac{c}{Ag} \ . \tag{19}$$

The temperature profiles indicate that the main shock forms in the region $1 < z/L_s < 3$ and then rapidly increases in strength as it propagates down the hydrostatic density gradient. The Mach number of the shock, M_s, is evaluated

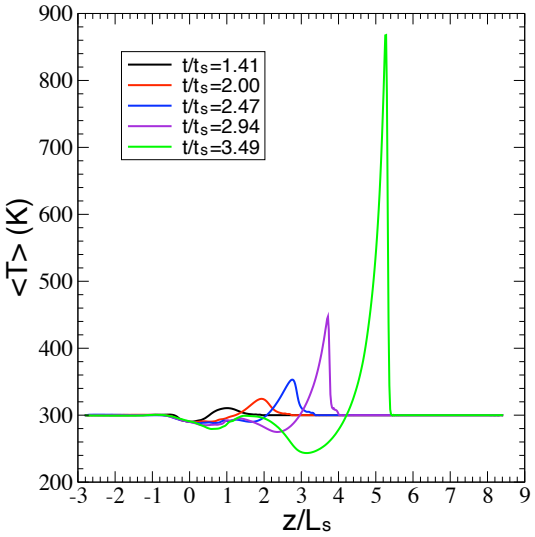

Fig. 3. Temperature profile at various times for the 3D Argon case.

from the temperature jump condition

$$\frac{\langle T \rangle_{\max}}{T_o} = \left[1 + \frac{2\gamma}{\gamma+1}(M_s^2 - 1)\right]\left[\frac{2 + (\gamma-1)M_s^2}{(\gamma+1)M_s^2}\right] \quad . \tag{20}$$

This jump condition provides a clear measure of shock strength and location, since T is initially constant. Shock Mach numbers versus height are plotted in Fig. 4 for all six simulations. In every case, $M_s \rightarrow 1$ as $z_s \rightarrow L_s$; hence, the main shock waves all begin to form at approximately a distance L_s above the interface. It is also apparent that the Argon and Neon simulations produce similar shocks, whereas the Krypton case produces a somewhat weaker shock. Additional tests (not shown) at various Atwood numbers indicate that for $A >\sim 0.5$ the Mach number curves nearly collapse; whereas, for lower Atwood numbers the curves gradually drop off. It is noteworthy that the 2D simulations all produce weaker shocks than their 3D counterparts. This may be a result of increased interaction among the shocklets in 3D compared to 2D, or it may be due to differences in 2D and 3D growth rates of the mixing layer [18].

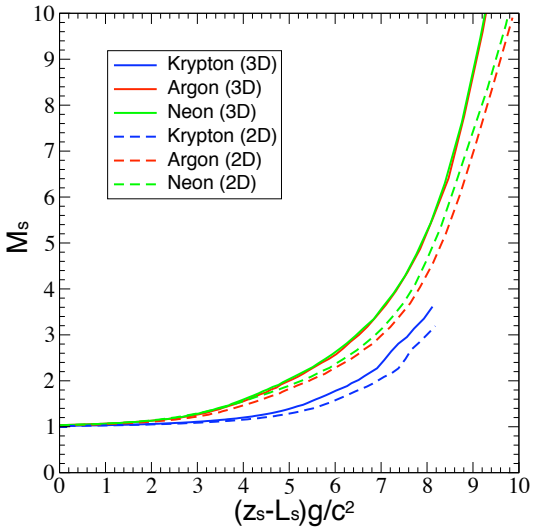

Fig. 4. Shock Mach number as a function of the nondimensional distance above the shock formation height.

Given the robust manner in which R-T instability produces shock waves, it is natural to ask why this phenomenon was not observed in earlier studies. In order to answer this question, consider the turbulent Mach number as defined by Mellado et al. [10],

$$M_t(z,t) \equiv \frac{\langle ||\mathbf{u}|| \rangle}{\langle c \rangle} \ . \tag{21}$$

This Mach number is plotted in Fig. 5 at late time for the 3D Argon case. The Atwood number for this case ($A = 0.533$) is close to the $A = 0.5$ simulations of Mellado et al. Mellado et al. used $M_t(0,t)$ as a gauge of compressibility effects. In their simulations, the distance from the interface to the top boundary of the domain was $2.8L_s$. From Fig. 5 it is apparent that this distance is too short to capture the true maximum of M_t. As a further illustration, $M_t(0,t)$ as well as the maximum value of M_t over all z are plotted in Fig. 6. At $t = 2.2t_s$, the Mach number just behind the shock overtakes the Mach number on the center

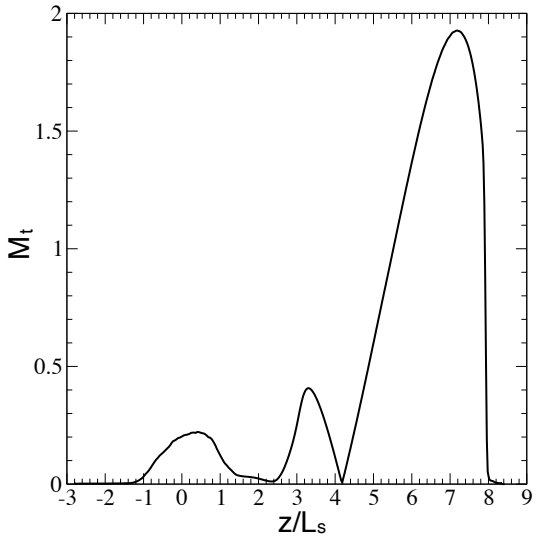

Fig. 5. Turbulent Mach number versus height at $t/t_s = 3.9$ for the 3D Argon case.

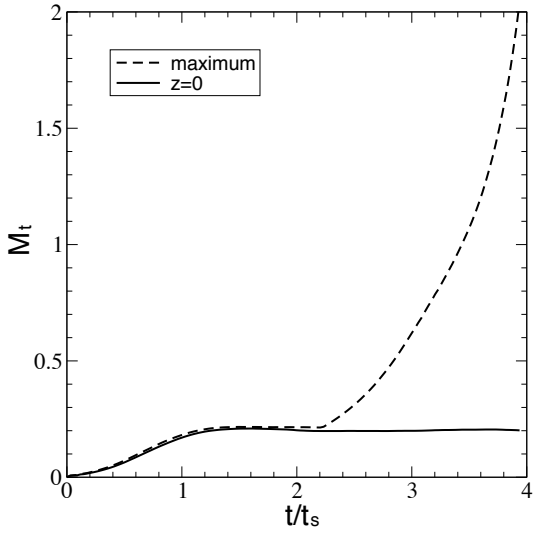

Fig. 6. Temporal evolution of the turbulent Mach number for the 3D Argon case.

plane and the two curves rapidly diverge. The turbulent Mach number on the center plane does not provide a reliable measure of compressibility effects at late time.

Finally, the present results raise the question as to whether R-T shocks could provide a detonation mechanism for type Ia supernovae. Relevant parameters for an exploding white dwarf are: $c \approx 7 \times 10^8\, cm/s$, $g \approx 10^{10}\, cm/s^2$ and $A \approx 0.2$; hence, a rough estimate of the shock formation length is $L_s \approx 2500\, km$. This is approximately the radius of the expanded star, which leaves some doubt as to whether the shock would be able to form. Thus far, our scoping simulations using a Helmholtz equation of state [19] have failed to produce a shock of sufficient strength to ignite the carbon.

Acknowledgements

We are grateful to Dr. W. H. Cabot for help in writing the code. This work was performed under the auspices of the U.S. Department of Energy by the University of California Lawrence Livermore National Laboratory under contract No. W-7405-Eng-48.

References

[1] F. X. Timmes. On the acceleration of nuclear flame fronts in white dwarfs. *ApJ*, 423:L131–L134, 1994.

[2] K. Nomoto, K. Iwamoto, and N. Kishimoto. Type Ia supernovae; their origin and possible applications in cosmology. *Science*, 276:1378–1382, 1997.

[3] E. J. Lentz, E. Baron, and D. Branch. Sn 1984a and delayed-detonation models fo type Ia supernovae. *ApJ*, 547:402–405, 2001.

[4] V. N. Gamezo, A. M. Khokhlov, and E. S. Oran. Three-dimensional delayed-detonation model of type Ia supernovae. *ApJ*, 623:337–346, 2005.

[5] M. Zingale, S. E. Woosley, C. A. Rendleman, M. S. Day, and J. B.

Bell. Three-dimensional numerical simulations of Rayleigh-Taylor unstable flames in type Ia supernovae. *ApJ*, 632:1021–1034, 2005.

[6] W. H. Cabot and A. W. Cook. Reynolds number effects on Rayleigh-Taylor instability with possible implications for type Ia supernovae. *Nature Physics*, 2:562–568, 2006.

[7] F. K. Röpke and J. C. Niemeyer. Delayed detonations in full-star models of type Ia supernova explosions. *Astronomy and Astrophysics*, 464:683–686, 2007.

[8] J. Zhang, O. E. B. Messer, A. M. Khokhlov, and T. Plewa. On the evolution of thermonuclear flames on large scales. *ApJ*, 656:347–365, 2007.

[9] M. Zingale and L. J. Dursi. Propagation of the first flames in type Ia supernovae. *ApJ*, 656:333–346, 2007.

[10] J. P. Mellado, S. Sarkar, and Y. Zhou. Large-eddy simulation of Rayleigh-Taylor turbulence with compressible miscible fluids. *Phys. Fluids*, 17:076101, 2005.

[11] A. W. Cook. Artificial fluid properties for large-eddy simulation of compressible turbulent mixing. *Phys. Fluids*, 19:055103, 2007.

[12] A. W. Cook and P. E. Dimotakis. Transition stages of Rayleigh-Taylor instability between miscible fluids. *J. Fluid Mech.*, 443:69–99, 2001.

[13] J. D. Anderson. *Modern Compressible Flow.* McGraw Hill, 2004.

[14] R. Courant and K. O. Friedrichs. *Supersonic Flow and Shock Waves.* Interscience Publishers, New York, 1948.

[15] S. Chandrasekhar. *Hydrodynamic and Hydromagnetic Stability.* Oxford Univ. Press, Oxford, 1961.

[16] J. R. Ristorcelli and T. T. Clark. Rayleigh-Taylor turbulence: Self-similar analysis and direct numerical simulations. *J. Fluid Mech.*, 507:213–253,

2004.

[17] A. W. Cook, W. Cabot, and P. L. Miller. The mixing transition in Rayleigh-Taylor instability. *J. Fluid Mech.*, 511:333–362, 2004.

[18] W. Cabot. Comparison of two- and three-dimensional simulations of miscible Rayleigh-Taylor instability. *Phys. Fluids*, 18:045101, 2006.

[19] F. X. Timmes and F. D. Swesty. The accuracy, consistency, and speed of an electron-positron equation of state based on table interpolation of the helmholtz free energy. *The Astrophysical Journal Supplement Series*, 126:501–516, 2000.